PHYSICAL REVIEW E **96**, 032115 (2017)

Uhlenbeck-Ford model: Phase diagram and corresponding-states analysis

Rodolfo Paula Leite,* Pedro Antonio Santos-Flórez,† and Maurice de Koning‡
Instituto de Física "Gleb Wataghin", Universidade Estadual de Campinas, UNICAMP, 13083-859 Campinas, São Paulo, Brazil

(Received 7 April 2017; revised manuscript received 7 June 2017; published 11 September 2017)

Using molecular dynamics simulations and nonequilibrium thermodynamic-integration techniques we compute the Helmholtz free energies of the body-centered-cubic (bcc), face-centered-cubic (fcc), hexagonal close-packed, and fluid phases of the Uhlenbeck-Ford model (UFM) and use the results to construct its phase diagram. The pair interaction associated with the UFM is characterized by an ultrasoft, purely repulsive pair potential that diverges logarithmically at the origin. We find that the bcc and fcc are the only thermodynamically stable crystalline phases in the phase diagram. Furthermore, we report the existence of two reentrant transition sequences as a function of the number density, one featuring a fluid-bcc-fluid succession and another displaying a bcc-fcc-bcc sequence near the triple point. We find strong resemblances to the phase behavior of other soft, purely repulsive systems such as the Gaussian-core model (GCM), inverse-power-law, and Yukawa potentials. In particular, we find that the fcc-bcc-fluid triple point and the phase boundaries in its vicinity are in good agreement with the prediction supplied by a recently proposed corresponding-states principle [J. Chem. Phys. **134**, 241101 (2011); Europhys. Lett. **100**, 66004 (2012)]. The particularly strong resemblance between the behavior of the UFM and GCM models are also discussed.

DOI: 10.1103/PhysRevE.96.032115

I. INTRODUCTION

Originally named Gaussian gas, the model devised by Uhlenbeck and Ford [1] was proposed to provide a system for which the virial equation of state could be handled analytically [2]. The model, here referred to as the Uhlenbeck-Ford model (UFM) to avoid confusion with the well-known Gaussian-core model (GCM), is characterized by an ultrasoft, purely repulsive pairwise interaction potential that diverges logarithmically at the origin and features an energy scale that coincides with the thermal energy unit $k_B T$, with k_B Boltzmann's constant and T the absolute temperature. The particular functional form of the potential permits, in principle, that the virial coefficients and, therefore, the equation of state and excess free energies for the fluid phase be evaluated analytically. Moreover, Baram and Rowlinson [3], based on the convergence properties of the virial expansion, argued that the fluid is the only thermodynamically stable phase for the UFM, regardless of the number density.

These properties motivated a recent investigation into the suitability of the UFM to serve as a reference system for fluid-phase free-energy computations [4]. The results demonstrate that, while the original UFM is too soft to be useful, the scaling of the energy unit $k_B T$ by a factor p provides a convenient reference system for values of $p \sim 50$–100. However, although the original model characterized by $p = 1$ exists only in the fluid phase, the phase behavior for $p \neq 1$ is not known. Therefore, to assess the regions of applicability of the UFM as a reference system in free-energy computations for fluid-phase systems, knowledge of its phase diagram is required.

Moreover, such knowledge is also of interest from a more general point of view, for instance, in the context of understanding the generic phase behavior of systems characterized by soft purely repulsive pairwise interactions. This class of systems, aside from the UFM, includes the GCM [5–9], the inverse-power-law (IPL) interaction [7,10–18], and the Yukawa-type potentials [19–23]. Indeed, invoking a corresponding-states principle, Khrapak *et al.* [24] have recently shown that the melting curves of various different pairwise interaction potentials display universal behavior, collapsing to the near vicinity of a master curve when using appropriately selected scaled variables. In particular, based on the same principle, similar universal behavior has been observed for the location of face-centered-cubic (fcc)–body-centered-cubic (bcc)–fluid triple point for purely repulsive potentials [25]. Interestingly, even other kinds of pairwise interactions such as the Buckingham or exp-6 model [26], the Yoshida and Kamakura (YK) potentials [27–29], and the modified inverse-power potentials [29] show very similar phase behavior for low densities.

In this setting, the purpose of the present paper is the construction of the UFM's phase diagram. To this end we perform extensive molecular dynamics (MD) simulations using the nonequilibrium free-energy techniques to determine its phase behavior. Computing the Helmholtz free energies of the bcc, fcc, hexagonal close-packed (hcp), and fluid phases and applying the common-tangent procedure, we construct the phase diagram of the UFM under controlled conditions of the pressure and scaling factor p and locate the fcc-bcc-fluid triple point. Subsequently, the position of the latter is analyzed in further detail by using a finite-size scaling extrapolation procedure. Finally, the results are compared to those obtained for other purely-repulsive pair potentials within the context of the corresponding-states principle.

The remainder of the paper has been organized as follows. In Sec. II, we describe the UFM and summarize its principal characteristics, followed by a brief outline of the used nonequilibrium free-energy techniques and a description of the MD simulation details. In Sec. III, we present and discuss the results of the free-energy calculations for the solid and

---

*rleite@ifi.unicamp.br
†pasantos@ifi.unicamp.br
‡dekoning@ifi.unicamp.br

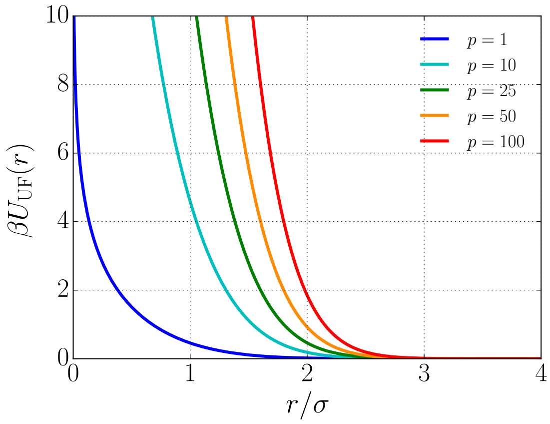

FIG. 1. Interatomic potential associated with the UFM for different values of p.

fluid phases as well as the corresponding phase behavior characteristics. Based on the results, we compare the phase diagram topology and location of the triple point for the UFM to those of the GCM, IPL, and Yukawa systems within the context of the corresponding-states principle proposed by Khrapak *et al.* [24,25]. We conclude with a summary in Sec. IV.

II. MODEL AND SIMULATION METHODS

A. The Uhlenbeck-Ford model

The UFM is defined by the interatomic pair potential,

$$U_{\mathrm{UF}}(r) = -\frac{p}{\beta}\ln\left(1 - e^{-(r/\sigma)^2}\right), \tag{1}$$

where $\beta \equiv (k_B T)^{-1}$, σ is a length-scale parameter, and $p > 0$ is a scaling factor. Figure 1 displays the UFM potential for a number of different scaling factors p. It is characterized by a smooth and purely repulsive soft-sphere interaction that diverges logarithmically as $r \to 0$ and decays rapidly for increasing distances. Increasing the value of p gives rise to a stronger repulsion.

Because of the temperature-dependent functional form of the interaction potential in Eq. (1), the partition function is independent of temperature and eliminates it as a relevant thermodynamic parameter in the model. On the other hand, given that the parameter p is a scaling factor of the potential energy, it plays the role of an effective inverse temperature T^*, with $T^* \equiv 1/p$. Furthermore, given that the pair potential is of the generic form

$$U(r) = \Phi(r/\sigma), \tag{2}$$

it can be shown [2] that the Helmholtz free energy per particle of a collection of N UFM particles confined to a volume V is a function of only adimensional variables and can be expressed in the form

$$\frac{\beta F_{\mathrm{UF}}}{N} = f(\rho\sigma^3, p), \tag{3}$$

with $\rho \equiv N/V$ the number density. In particular, as discussed recently [4], the virial-expansion expression for the excess free energy per particle of the fluid phase can be written as

$$\frac{\beta F_{\mathrm{UF}}^{\mathrm{exc}}(x,p)}{N} = \sum_{n=1}^{\infty} \frac{\tilde{B}_{n+1}(p)}{n} x^n, \tag{4}$$

where the $\tilde{B}_{n+1}(p)$ are reduced virial coefficients and x is the adimensional variable

$$x \equiv b\rho, \tag{5}$$

with $b \equiv \frac{1}{2}(\pi\sigma^2)^{3/2}$. Numerical values of the virial coefficients for several p's can be found in Ref. [4].

B. Free-energy calculations

For each phase we compute the Helmholtz free energy as a function of p on a predefined grid of x values, the set $\{x_i\}$, with $0.195 \leqslant x_i \leqslant 2.784$. In other words, for each phase we compute a collection of Helmholtz free-energy functions $F_{\mathrm{UF}}(p;x_i)$ of the scaling variable p at fixed x, one for each of the values in the set $\{x_i\}$.

Each free-energy function $F_{\mathrm{UF}}(p;x_i)$ is computed on an interval of p values $[p_l, p_u]$, where the lower and upper limits, p_l and p_u, are chosen so as to guarantee that the phase under consideration is at least metastable. In particular, for the considered crystalline phases, the upper limit is always chosen to be $p_u = 1000$. The values of the lower limit, on the other hand, are adjusted for each value of x so as to remain in the metastable regime. For the fluid phase, the lower limit is always set at $p_l = 50$, while the upper limit was chosen as large as possible while avoiding freezing transitions.

The free-energy functions are computed combining the reversible-scaling (RS) path [30,31] and the adiabatic switching (AS) approach [32–34]. In this scheme, the Helmholtz free energy as a function of p is computed as

$$F_{\mathrm{UF}}(p;x_i) = F_{\mathrm{UF}}(p_0;x_i) + W_{\mathrm{rev}}(p;x_i), \tag{6}$$

where $F_{\mathrm{UF}}(p_0;x_i)$ is the Helmholtz free-energy at scaling factor p_0, and W_{rev} is the work done on the system during a reversible process in which the scaling factor in the potential varies from p_0 to p. This process is described by the switching Hamiltonian,

$$H(\lambda) = \sum_{i=1}^{N} \frac{\mathbf{p}_i^2}{2m} - \frac{\lambda}{\beta}\sum_{i>j} \ln\left[1 - e^{-(r_{ij}/\sigma)^2}\right], \tag{7}$$

where N is the number of particles, and the $\mathbf{p}_i$ denotes the particle momenta. The reversible work $W_{\mathrm{rev}}(p;x_i)$ is given by the well-known relation

$$W_{\mathrm{rev}}(p;x_i) = \int_{p_0}^{p} \left\langle \frac{\partial H}{\partial \lambda} \right\rangle d\lambda, \tag{8}$$

where the angular brackets denote canonical equilibrium ensemble averages at fixed values of β, x_i, and λ. In the AS approach, the reversible-work integral is estimated along an explicitly time-dependent process in which $\lambda = \lambda(t)$, according to

$$W_{\mathrm{dyn}}(p;x_i) = \int_{0}^{t_p} \left(\frac{\partial H}{\partial \lambda}\right) \frac{d\lambda}{dt} dt, \tag{9}$$

where t_p is the duration of the dynamical process in which λ varies between p_0 and p and the integral is over instantaneous values of the thermodynamic driving force $\partial H/\partial\lambda$ along the process.

Due to the intrinsic nonequilibrium nature of these processes, W_{dyn} is a stochastic variable whose mean value $\overline{W}_{\text{dyn}}$, determined by averaging over a set of different realizations of the process, overestimates the reversible work, i.e.,

$$\overline{W}_{\text{dyn}} \geqslant W_{\text{rev}}, \tag{10}$$

with the equality being valid only in the limit of an infinitely slow, quasistatic process. However, if the process is sufficiently slow for linear-response theory to be valid, the systematic error can be eliminated by combining the results of forward and backward processes [35]; i.e.,

$$W_{\text{rev}}(p) = \tfrac{1}{2}\big[\overline{W}_{\text{dyn}}^{p_0\to p} - \overline{W}_{\text{dyn}}^{p\to p_0}\big]. \tag{11}$$

In this manner, the reversible work function $W_{\text{rev}}(p;x_i)$ in Eq. (6) is determined by carrying out a number of replicas of the nonequilibrium process in which λ varies in the interval $[p_l,p_u]$, in both directions. $W_{\text{rev}}(p;x_i)$ is estimated by combining the forward and backward results as prescribed by Eq. (11).

Finally, to find the final Helmholtz free energy $F_{\text{UF}}(p;x_i)$ using Eq. (6), one needs to determine the reference value $F_{\text{UF}}(p_0;x_i)$. For the crystalline phases, it is determined for $p_0 = p_u = 1000$ using the standard Frenkel-Ladd (FL) [31,36] switching path to the Einstein crystal in combination with the AS approach in forward and backward process directions. For the fluid phase, on the other hand, we use the known Helmholtz free-energy values for $p_0 = p_l = 50$ as computed in Ref. [4].

C. Common-tangent construction

To construct the phase diagram in terms of pressure and scaling factor p, we adopt the common-tangent procedure to determine the values of p at which the pressure and chemical potentials of two phases are equal. This is achieved as follows. Using the Helmholtz free-energies as a function of p for the set of densities $\{x_i\}$, i.e., the functions $F_{\text{UF}}(p;x_i)$ described in Sec. II B, we construct a set of Helmholtz free energies $F_{\text{UF}}(v;p_i)$ as a function of the volume per particle $v = b^3/x$ for a particular set $\{p_i\}$ of scaling factor values. Subsequently, each of these curves is adjusted to a third-degree polynomial by means of a least-squares regression analysis, followed by the determination of the common tangent and corresponding per-particle volumes for pairs of phases. This procedure is carried out for a predefined grid of p-values in the set $\{p_i\}$, with $50 \leqslant p_i \leqslant 1000$.

D. Simulation details

All MD simulations have been carried out using the `LAMMPS` code [37]. The phase diagram reported in the next section was obtained using cubic computational cells containing $\sim 10^4$ particles, subject to standard periodic boundary conditions. A Langevin thermostat with a damping time scale of 100 time steps was used to control the temperature at 1000 K and, choosing a particle mass of 100 g/mol, the equations of motion were integrated using the velocity-Verlet algorithm with a timestep $\Delta t = 1$ fs. The UF length-scale was set at $\sigma = 1.0$ Å, and a cutoff radius of $r_c = 4.0\,\sigma$ was adopted.

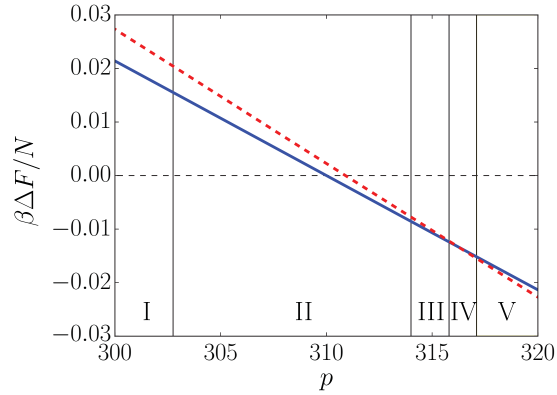

FIG. 2. Helmholtz free energies per particle of fcc (red dashed line) and bcc phase (blue line) relative to that of the fluid as a function of p for $x = 0.2673$. The areas I, III, and V represent the intervals of p values where, respectively, the fluid, bcc, and fcc forms are the thermodynamically stable phases as determined using the common-tangent construction. Regions II and IV depict the intervals of fluid-bcc and bcc-fcc coexistence, respectively (see text). The values of the excess Helmholtz free energies of fluid, bcc, and fcc phases at the three crossing points are $\beta F^{\text{exc}}_{\text{fluid}}/N = \beta F^{\text{exc}}_{\text{bcc}}/N = 7.42531 \pm 0.00006$ and $\beta F^{\text{exc}}_{\text{fcc}}/N = 7.42587 \pm 0.00003$ for $p = 309.9$, $\beta F^{\text{exc}}_{\text{fluid}}/N = \beta F^{\text{exc}}_{\text{fcc}}/N = 7.44544 \pm 0.00006$ and $\beta F^{\text{exc}}_{\text{bcc}}/N = 7.44352 \pm 0.00008$ for $p = 310.9$, and $\beta F^{\text{exc}}_{\text{fluid}}/N = 7.56563 \pm 0.00006$ and $\beta F^{\text{exc}}_{\text{bcc}}/N = \beta F^{\text{exc}}_{\text{fcc}}/N = 7.55066 \pm 0.00008$ for $p = 316.2$.

To compute the absolute Helmholtz free-energy for the bcc, fcc, and hcp phases for $p_0 = 1000$ we perform 10 independent forward and backward FL switching processes at fixed center of mass, using the polynomial $\lambda(t)$ protocol given in Ref. [31]. To reduce dissipation [31], the force constants of the Einstein crystal are chosen such that the mean-square displacement of the Einstein oscillators closely matches those of the particles in the crystalline UFM phase. Before each FL process, the system is first equilibrated during a time interval $t_{\text{eq}} = 10^5\Delta t$, followed by the switching procedure carried out in the switching time $t_{\text{sw}} = 10^6\Delta t$. Following the procedures detailed in Ref. [31] we verified that this value is sufficiently large for linear response theory to hold and the reversible-work estimator Eq. (11) to be valid.

A similar procedure was adopted for the RS simulations of the bcc, fcc, hcp, and fluid phases. We carried out 10 independent forward and backward RS simulations for each process, using a linear $\lambda(t)$ protocol. The employed equilibration and switching times were the same as those used in the FL switching runs. As for the FL calculations, these choices are sufficient for the processes to be in the linear-response regime.

III. RESULTS AND DISCUSSION

A. Phase diagram

Figure 2 depicts typical results for the Helmholtz free energies $F_{\text{UF}}(p;x_i)$ as a function of the scaling parameter p for given x, displaying the bcc and fcc Helmholtz free energies per particle relative to that of the fluid for $x = 0.2673$. There are three p values at which the Helmholtz free energies of

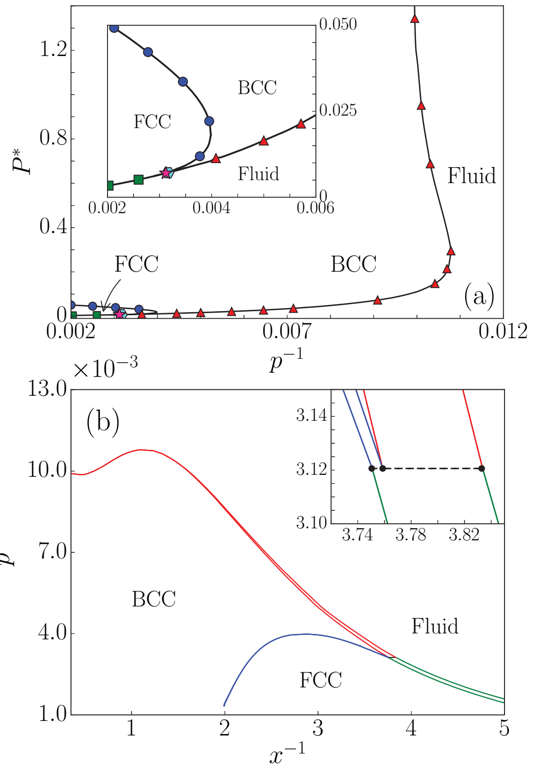

FIG. 3. (a) Phase diagram of the UFM in the (P^*, p) plane, with P^* the reduced pressure defined as $P^* \equiv \beta P \sigma^3/p$. Symbols represent points of equal chemical potential for specific pairs of phases: bcc-fluid, bcc-fcc, and fcc-fluid pairs are depicted by red triangles, blue circles and green squares, respectively. Error bars are smaller than symbol size. Black lines are cubic-spline curves that serve as guides to the eye. Pink star represents the location of the triple point. Light blue hexagon depicts triple-point position obtained after finite-size scaling analysis (see text). Inset provides a zoom of the triple-point region. (b) Phase diagram of the UFM in the (x, p) plane. Green, blue and red lines delimit fcc-fluid, fcc-bcc, and bcc-fluid coexistence regions, respectively. Inset provides a zoom of the triple-point region, where the dashed line represents the width of the triple point.

two phases are equal, one for fluid-bcc pair near $p = 309.9$, another for the fluid-fcc pair near $p = 310.9$, and a third for the bcc and fcc phases close to $p = 316.5$. Furthermore, the areas numbered I through V represent intervals of p values that describe different regions of thermodynamic phase stability for this particular value of x, as determined using the common-tangent construction further discussed below. In addition to the bcc and fcc phases, we also considered other crystalline structures such as the hcp, diamond-cubic and simple-cubic crystals. While the hcp phase is found to be only metastable, the other two were found to be not even mechanically stable under any conditions of x and p.

Subsequently, to determine the coexistence lines of the UFM phase diagram, we apply the common-tangent construction described in Sec. II C to the Helmholtz free-energy data for the entire range of p values between $50 \leqslant p_i \leqslant 1000$. The resulting diagram for controlled conditions of the scaling factor p and the pressure is shown in Fig. 3(a). It is characterized by the existence of a single fluid phase and two crystalline forms, i.e., the bcc and fcc phases. Each symbol type represents coexistence points of equal pressure and chemical potentials for specific pairs of phases, with the triangles, circles, and squares representing the fluid-bcc, bcc-fcc, and fluid-fcc coexistence, respectively. The three coexistence lines meet at a triple point and its coordinates are estimated by determining the crossing points of cubic spline fits to the fluid-bcc, bcc-fcc, and fluid-fcc phase boundaries, locating it at a reduced pressure $P_t^* \equiv \beta P_t \sigma^3/p = (7.0 \pm 0.2)\times 10^{-3}$ and a p value $p_t = 320 \pm 2$. The error bars depict typical variations in the results when using different sets of data points in the spline fits for the phase boundaries. Figure 3(b) displays the phase diagram of the UFM in (x, p) representation, displaying the widths of the coexistence regions.

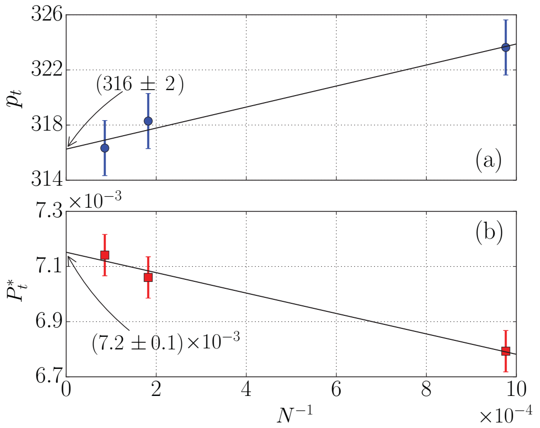

FIG. 4. Finite-size scaling of the fcc-bcc-fluid Helmholtz free-energy triple point. (a) Linear scaling of p_t as a function of $1/N$. Blue circles represent data for p_t obtained from simulations and line is the best linear fit. (b) Linear scaling of P_t^* as a function of $1/N$. Red squares represent data obtained from simulations and line is the best linear least-squares fit.

To assess the influence of the finite size of the simulation cells, we have repeated the calculations for three cell sizes containing particle numbers $N = 1024$, 5488, and 11 664, respectively, for all three phases. The corresponding results for the triple point are shown in Fig. 4, plotting the triple-point coordinates as a function of $1/N$. The scaling is approximately linear for both P_t^* and p_t, allowing an extrapolation of the triple point position to the $N \to \infty$, giving $P_t^* = (7.2 \pm 0.1)\times 10^{-3}$ and $p_t = 316 \pm 2$. This extrapolated result is shown as the light-blue hexagon in Fig. 3(a).

The choice of a finite interaction cutoff at $r_c = 4.0\sigma$ is also found to have a negligible influence on the results. Using the same cells as those used to construct the phase diagram we recomputed the Helmholtz free energies for fcc, bcc, and fluid phases in the vicinity of the triple point for an increased cutoff radius of 5.0σ. The relative differences between the free-energy values for both cutoffs are found to be no larger than 2.0×10^{-4}.

B. Discussion

The phase diagrams of the UFM in Fig. 3 are very similar to those seen in other systems characterized by purely-repulsive interactions, such as the GCM, Yukawa, and IPL models. All of these feature phase diagrams contain a single fluid

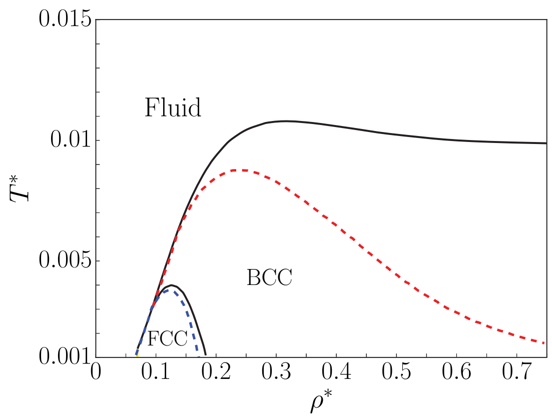

FIG. 5. Comparison between the phase diagrams of the UFM and GCM in the (ρ^*, T^*) representation. Black lines are cubic-spline curves representing the coexistence conditions for the UFM. On the displayed scale the thickness of the black lines is larger than widths of the coexistence regions. Red and blue dashed lines represent the coexistence conditions for the GCM as obtained from Ref. [8].

TABLE I. Scaled variables s and $\mathcal{F}$ at the triple points for the GCM, IPL, Yukawa, and UFM models. The numerical values for the first three have been reproduced from Table 1 in Ref. [25]. The UFM results were obtained using the triple-point location present in Fig. 3.

Model	s_t	$\mathcal{F}_t$
GCM	0.129	24.08
IPL	0.14	28.46
IPL	0.16	31.57
Yukawa	0.145	31.26
Yukawa	0.142	27.65
Yukawa	0.128	27.09
UFM	0.13	25.29

phase and the fcc and bcc crystalline forms. The resemblance with the GCM is particularly striking [8], displaying the same two reentrant transition sequences as can be seen in Fig. 5. Specifically, there is a fluid-bcc-fluid reentrant melting transition as the density is increased for values of p close to 100, i.e., $T^* \equiv 1/p$ close to 0.01, and a bcc-fcc-bcc-fluid sequence in the vicinity of the triple-point region. On the other hand, in contrast to the case of the GCM, for increasing densities the bcc structure remains the stable thermodynamic phase and does not remelt into the fluid.

Prestipino and coworkers [8] discussed the similarities between the phase behaviors of various model systems characterized by soft repulsive interactions. Specifically, they established a criterion to relate the phase behaviors of the IPL and Yukawa models to that of the GCM by requiring that the logarithmic derivatives of the corresponding potentials be equal to that of the GCM for interparticle separations close to the mean distance $\Delta = \rho^{-1/3}$, providing mapping values of potential parameters that play the role that of an effective temperature.

More recently, Khrapak and coworkers [24,25] proposed a corresponding-states principle by which the melting curves and fcc-bcc-fluid triple points of various different pairwise interaction potentials are shown to display universal behavior when using appropriately selected scaled variables. For a pair potential $U(r)$, these variables are the generalized *softness* parameter,

$$s = [-1 - U''(\Delta)\Delta/U'(\Delta)]^{-1}, \tag{12}$$

and the generalized *interaction* (or reduced force) parameter,

$$\mathcal{F} = -\beta\, U'(\Delta)\Delta, \tag{13}$$

where $\Delta \equiv \rho^{-1/3}$ is the mean interparticle distance. Using the functional form of Eq. (1), the corresponding expressions for the UFM are

$$s = -\frac{1}{2}\left[1 - \left(\frac{\Delta}{\sigma}\right)^2 \frac{e^{(\Delta/\sigma)^2}}{(e^{(\Delta/\sigma)^2} - 1)}\right]^{-1}, \tag{14}$$

and

$$\mathcal{F} = \left(\frac{2p}{e^{(\Delta/\sigma)^2} - 1}\right)\left(\frac{\Delta}{\sigma}\right)^2. \tag{15}$$

Using these definitions, one can determine the values of the variables s_t and $\mathcal{F}_t$ that correspond to the triple point. Table I presents these values for the GCM, IPL, Yukawa, and UFM systems, where the data for the former three have been reproduced from Table I in Khrapak and Morfill [25]. To compute these parameters for the UFM, we have used the triple-point result from Fig. 3, using $p = 320$ and a mean interparticle distances Δ that corresponds to the average density across the coexistence interval, i.e., $x = 0.26377$. They observed that the scaled variables s_t and $\mathcal{F}_t$ display only a relatively narrow range of values between these models, with $s_t \simeq 0.14 \pm 0.02$ and $\mathcal{F}_t \simeq 28 \pm 4$. We find that the corresponding values for the UFM also fall within these intervals. Specifically, when using the above-mentioned values of x and p for the UFM, one finds $s_t = 0.13$ and $\mathcal{F}_t = 25.29$. As argued in Ref. [25] this proximity of values for different potentials suggests the existence of a corresponding-states principle that allows the triple-point regions of different model systems to be *approximately* located by finding the thermodynamic conditions that satisfy $s_t^c \simeq 0.14$ and $\mathcal{F}_t^c \simeq 28$. Doing so for the UFM one finds the corresponding-states triple point to be at $p_t^c = 281.7$ and $x_t^c = 0.289574$, which is fairly close to the triple point obtained in the simulations.

In addition to the position of the fcc-bcc-fluid triple point itself, the universal-like behavior also appears for the phase boundary lines near the triple point. Again following Khrapak *et al.* [24,25], this can be seen if one plots the fluid-solid and bcc-fcc boundaries in terms of the scaled variables s/s_t and $\mathcal{F}/\mathcal{F}_t$, as has been done in Fig. 6 for the GCM, IPL, Yukawa, and UFM systems, respectively. The numerical results for the GCM have been taken from Refs. [7], those for the IPL data from Refs. [7,11], and the Yukawa data from Refs. [20,21]. Representing the phase diagrams in this manner, it becomes clear that the GCM, Yukawa, and IPL have topologically equivalent phase diagrams near the triple point, where it separates a region in which the fluid freezes directly into the fcc phase to another in which the bcc structure is intermediate. Moreover, the rescaled melting lines of all three previously considered models collapse essentially on a single master melting curve, described by $\mathcal{F}(s) \simeq 106\, s^{2/3}$ [24,25].

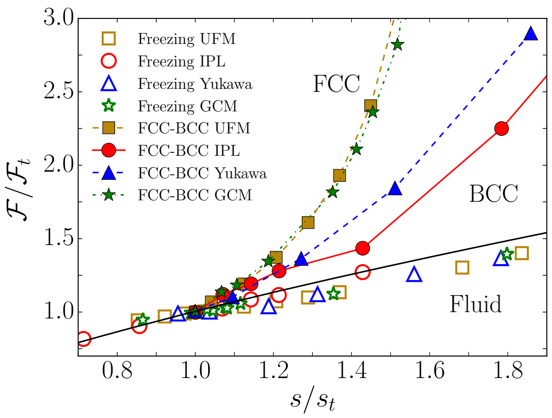

FIG. 6. Phase boundaries in the vicinity of the fcc-bcc-fluid triple point of the UFM, GCM, IPL, and Yukawa systems on the plane of reduced parameters s/s_t and $\mathcal{F}/\mathcal{F}_t$. The black solid curve corresponds to the universal melting curve $\mathcal{F}(s) \simeq 106\, s^{2/3}$ [24]. Open symbols correspond to the fluid-solid phase transitions and the solid symbols represent the fcc-bcc phase transition. (For data references, see the text).

Our results here show that the phase behavior of the UFM is equivalent to the other three and is consistent with the corresponding-states principle.

In particular, comparing the rescaled phase behavior to that of the other three models it is evident that the UFM is most similar to the GCM. Indeed, both the rescaled melting curves as well as the bcc-fcc boundaries lines essentially fall on top of each other. Following Ref. [25], this similarity between the UFM and GCM also manifests itself when plotting the potential-energy functions of the models in the vicinity of the triple point in terms of the rescaled form,

$$u(r/\Delta) \equiv \beta U(r/\Delta), \tag{16}$$

and where the potential parameters have been set such that $s = 0.14$ and $\mathcal{F} = 28$. The results are shown in Fig. 7. While the GCM, IPL, and Yukawa potentials touch only at a single point around $x \simeq 0.85$, the GCM and UFM essentially overlap across the entire region $x \gtrsim 0.7$. Only for shorter distances, for which the GCM tends to a constant whereas the UFM diverges, do the potential-energy expressions deviate substantially. This resemblance becomes more explicit when writing the potential-energy function in Eq. (1) in terms of its Taylor series representation,

$$U_{\rm UF}(r) = \frac{p}{\beta}\sum_{k=1}^{\infty}\frac{e^{-k(r/\sigma)^2}}{k} = \frac{p}{\beta}e^{-(r/\sigma)^2}\left[1+\frac{1}{2}e^{-(r/\sigma)^2}+\cdots\right], \tag{17}$$

which converges for any $r \geqslant 0$. Except for small values of r/σ, the predominant term in the series corresponds to the GCM. This implies that, as the density of the system is reduced, the behavior of the UFM and the GCM should become progressively more alike. For high densities, on the other hand, it is expected that the two models display different phase behavior. This indeed appears to be the case. While the bcc phase in the GCM melts for any energy scale as long as the system is sufficiently dense, our results indicate that the bcc phase in the UFM is stable for arbitrarily high densities for $p \gtrsim 100$.

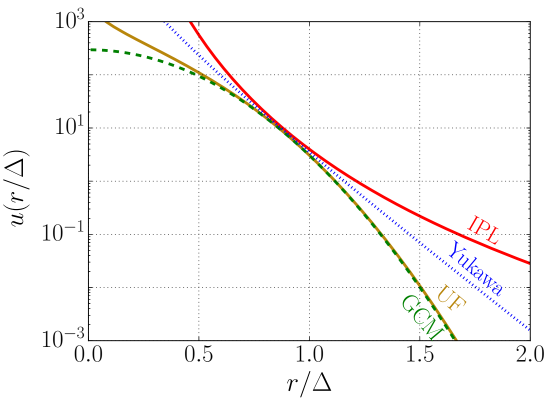

FIG. 7. Rescaled potential energy functions in the vicinity of the triple point for the IPL, Yukawa, GCM, and UFM models, with model parameters corresponding to $s = 0.14$ and $\mathcal{F} = 28$.

IV. SUMMARY

In summary, we have determined the phase diagram of the UFM using state-of-the-art nonequilibrium free-energy calculation techniques. Similar to other soft purely repulsive systems, we find the phase diagram to contain a single fluid phase and the crystalline bcc and fcc structures, the three of which can coexist at a triple point. The hcp phase is only metastable with respect to the fcc phase and other crystalline phases are found to not even be mechanically stable.

Using a finite-size scaling procedure, we determine the location of the fcc-bcc-fluid triple point and analyze its position as well as the phase boundaries in its vicinity in terms of the corresponding-states principle proposed by Khrapak *et al.* [24,25]. Applying its scaling approach, it is found that the UFM phase behavior is very similar to that of the GCM, IPL, and Yukawa systems. The UFM is particularly resemblant of the GCM, with their melting curves and bcc-fcc phase boundaries effectively overlapping. This similarity can be traced back to the particular functional form of the UFM, which can be written in terms of an infinite series of Gaussians. Its first term corresponds to the GCM and, except for large densities, dominates the value of the UFM potential-energy function. For large densities, on the other hand, all terms contribute and give rise to the logarithmic divergence of the UFM. It is suggested that this is related to the fact that, while the GCM is expected to melt as the density is increased, the UFM displays a stable bcc phase for arbitrarily high densities.

ACKNOWLEDGMENTS

We gratefully acknowledge support from the Brazilian agencies CNPq, Fapesp, Capes, and the Center for Computational Engineering and Sciences-Fapesp/Cepid Grant No. 2013/08293-7. Part of the calculations were performed at CCJDR-IFGW-UNICAMP and CENAPAD-SP. The authors acknowledge the National Laboratory for Scientific

Computing (LNCC/MCTI, Brazil) for providing HPC resources of the SDumont supercomputer, which have contributed to the research results reported in this paper. URL: http://sdumont.lncc.br

[1] G. Uhlenbeck and G. Ford, in *Studies in Statistical Mechanics—The Theory of Linear Graphs with Application to the Theory of the Virial Development of the Properties of Gases*, edited by G. E. Uhlenbeck and J. de Boer (North-Holland, Amsterdam, 1962), Vol. 2.

[2] D. McQuarrie, *Statistical Mechanics* (University Science Books, Sausalito, CA, 2000).

[3] A. Baram and J. Rowlinson, Mol. Phys. **74**, 707 (1991).

[4] R. Paula Leite, R. Freitas, R. Azevedo, and M. de Koning, J. Chem. Phys. **145**, 194101 (2016).

[5] F. H. Stillinger, J. Chem. Phys. **65**, 3968 (1976).

[6] A. Lang, C. N. Likos, M. Watzlawek, and H. Löwen, J. Phys.: Condens. Matter **12**, 5087 (2000).

[7] S. Prestipino, F. Saija, and P. V. Giaquinta, J. Chem. Phys. **123**, 144110 (2005).

[8] S. Prestipino, F. Saija, and P. V. Giaquinta, Phys. Rev. E **71**, 050102 (2005).

[9] C. E. Zachary, F. H. Stillinger, and S. Torquato, J. Chem. Phys. **128**, 224505 (2008).

[10] A. S. Bharadwaj and Y. Singh, Phys. Rev. E **95**, 032120 (2017).

[11] D. H. E. Dubin and H. Dewitt, Phys. Rev. B **49**, 3043 (1994).

[12] W. G. Hoover, M. Ross, K. W. Johnson, D. Henderson, J. A. Barker, and B. C. Brown, J. Chem. Phys. **52**, 4931 (1970).

[13] W. G. Hoover, D. A. Young, and R. Grover, J. Chem. Phys. **56**, 2207 (1972).

[14] W. G. Hoover, S. G. Gray, and K. W. Johnson, J. Chem. Phys. **55**, 1128 (1971).

[15] B. B. Laird and A. Haymet, Mol. Phys. **75**, 71 (1992).

[16] R. Agrawal and D. A. Kofke, Phys. Rev. Lett. **74**, 122 (1995).

[17] R. Agrawal and D. A. Kofke, Mol. Phys. **85**, 23 (1995).

[18] D. C. Wang and A. P. Gast, J. Chem. Phys. **110**, 2522 (1999).

[19] S. Hamaguchi, R. T. Farouki, and D. H. E. Dubin, J. Chem. Phys. **105**, 7641 (1996).

[20] S. Hamaguchi, R. T. Farouki, and D. H. E. Dubin, Phys. Rev. E **56**, 4671 (1997).

[21] R. S. Hoy and M. O. Robbins, Phys. Rev. E **69**, 056103 (2004).

[22] A. P. Hynninen and M. Dijkstra, Phys. Rev. E **68**, 021407 (2003).

[23] E. J. Meijer and D. Frenkel, J. Chem. Phys. **94**, 2269 (1991).

[24] S. A. Khrapak, M. Chaudhuri, and G. E. Morfill, J. Chem. Phys. **134**, 241101 (2011).

[25] S. A. Khrapak and G. E. Morfill, Europhys. Lett. **100**, 66004 (2012).

[26] G. Malescio, F. Saija, and S. Prestipino, J. Chem. Phys. **129**, 241101 (2008).

[27] F. Saija, S. Prestipino, and G. Malescio, Phys. Rev. E **80**, 031502 (2009).

[28] S. Prestipino, F. Saija, and G. Malescio, J. Chem. Phys. **133**, 144504 (2010).

[29] G. Malescio and F. Saija, J. Phys. Chem. B **115**, 14091 (2011).

[30] M. de Koning, A. Antonelli, and S. Yip, Phys. Rev. Lett. **83**, 3973 (1999).

[31] R. Freitas, M. Asta, and M. de Koning, Comput. Mater. Sci. **112**, 333 (2016).

[32] M. Watanabe and W. P. Reinhardt, Phys. Rev. Lett. **65**, 3301 (1990).

[33] M. de Koning and A. Antonelli, Phys. Rev. E **53**, 465 (1996).

[34] M. de Koning and A. Antonelli, Phys. Rev. B **55**, 735 (1997).

[35] M. de Koning, J. Chem. Phys. **122**, 104106 (2005).

[36] D. Frenkel and A. J. C. Ladd, J. Chem. Phys. **81**, 3188 (1984).

[37] S. Plimpton, J. Comput. Phys. **117**, 1 (1995).